ACS APPLIED MATERIALS & INTERFACES

www.acsami.org

Research Article

Constructed Self-Powered Electrostatic Nanofiber Membrane Coupled Piezoelectricity with Adhesive Strategy and Its Application in Efficient Capture of Bioaerosol

Feihong Xue, Guiying Li, Linghui Peng, Jianhua Qi, Zhishu Liang, Jiani Wang, Simeng Zhang, Huijun Zhao, and Taicheng An*

Cite This: *ACS Appl. Mater. Interfaces* 2026, 18, 41004–41016

Read Online

ACCESS | Metrics & More | Article Recommendations | Supporting Information

ABSTRACT: Among bioaerosols, viral aerosols, characterized by their small size (<300 nm), prolonged atmospheric suspension, and high infectivity, pose significant environmental and public health risks, particularly in densely populated or poorly ventilated areas. Herein, we developed an efficient method for viral aerosol capture and subsequent quantification based on an electrostatic adhesive nanofibrous membrane, which was fabricated by synergistically combining piezoelectric $BaTiO_3$-doped polystyrene with a polydopamine (PDA) surface coating. Conventional biosamplers are typically limited to flow rates below 6 L min^{-1} for efficient virus capture. In contrast, the designed self-powered electrostatic fiber membrane maintains >90% capture efficiency at flow rates up to 15 L min^{-1}, exhibiting a maximum static voltage of about 2 V under airflow disturbance. The PDA coating provides humidity-resistant capture, maintaining an efficient capture efficiency under different atmospheric conditions (relative humidity ranging from 40%–90%), further confirming the environmental adaptability of these home-made fibrous membranes. Moreover, under actual atmospheric conditions, the capture performance of these membranes surpasses commercial ones. Molecular dynamics simulation further proved that PDA coating could significantly enhance virus-binding affinity, and the captured virus can be efficiently eluted under mild acidic conditions. This breakthrough enables effective viral aerosol capture and subsequent quantification for environmental monitoring.

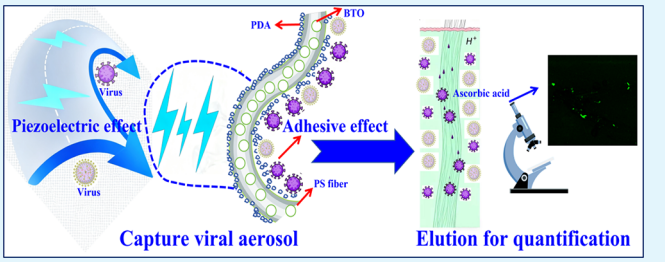

KEYWORDS: *bioaerosol capture, viral aerosol, capturing technology, electrostatic fiber membrane, adhesion strategy*

1. INTRODUCTION

Bioaerosols, comprising airborne microorganisms and their metabolite, pose significant public health risks.[1,2] Viral particles are especially notorious as infectious and highly pathogenic microorganisms in bioaerosols.[3] Recently, the global impact of viral aerosol transmission exemplified by SARS, influenza, and SARS-CoV-2 pandemics has underscored the urgent need for reliable monitoring methods to quantify viral aerosol during outbreaks of the epidemic.[4,5] In the actual atmospheric environment, the capture of viral aerosols poses a dual challenge.[6,7] Their small size (20–300 nm) renders individual suspended viral particles, while those attached to larger airborne particles[8,9] are susceptible to detachment and transfer during capturing. These intrinsic properties of small size, low mass, and transferability promote motion trajectories dominated by sampling pumps, thus significantly challenging conventional filtration, impaction, and cyclone-based capture methods. Therefore, the development of a new method to achieve efficient capture of viral aerosols is of great significance for revealing its actual airborne presence.

Sampling and measurement have been the most critical issues of viral aerosol monitoring.[10] However, limited by the inefficiency of conventional sampling techniques (quartz filter, cyclone, impactor, etc.) to capture airborne viruses (<10%), little is known about their actual presence in the atmosphere.[11−15] Currently, capture methods based on laminar-flow water-based condensation and electrostatic technologies are the most effective methods reported for viral aerosol.[16−19] However, all the above-mentioned methods have the drawback of limited sampling flow (typically <6 L min^{-1}).[17,20] As a result, the low collection flow velocity achieved by current methods leads to insufficient viral uptake, making it difficult to meet the requirements of rapid and accurate quantification for viral aerosol.

Received: May 9, 2026
Revised: July 4, 2026
Accepted: July 9, 2026
Published: July 15, 2026

https://doi.org/10.1021/acsami.6c09491
ACS Appl. Mater. Interfaces 2026, 18, 41004–41016

These challenges highlight the necessity of developing new methodologies capable of efficiently capturing submicron viral particles while operating at larger flow velocities, while also enabling complete release of the captured viral particles with high efficiency to accurately assess viral aerosol presence.

Electrostatic nanofiber offers promising solutions to bioaerosol capture due to its advantages, including small fiber diameter, high specific surface area, inherent electrostatic properties, and exceptional filtration efficiency. Recently, pioneering researchers have performed the application of electrospun nanofibers in an attempt to counter the threat of atmospheric particles.[21−23] The mechanism of nanofibers capturing viruses mainly relies on electrostatic and physical interception based on small pores and electrostatic charge.[24] Yet, its application to bioaerosol capture for offline quantification analysis remains limited by key issues as follows: (i) environmental factor-induced rapid electrostatic charge dissipation after electrospinning,[24] (ii) the captured particle may fall off and transfer under airflow interference due to low adhesion strength,[25] and (iii) the inefficient elution for downstream analysis similar to that of ordinary bioaerosol sampling membranes has not been well solved either.[14]

Recent studies have explored long-lasting electrostatic materials, attempting to solve the problem of electrostatic attenuation. For example, high removal efficiency of $PM_{0.3}$ is accomplished by self-sustained electrostatic PVDF air filters with an exceptionally long-range electrostatic property of aeolian vibration.[26] A self-sustained polyimide/silver fiber with long-lasting electrostatic force can remove 99.1% of $PM_{0.3}$.[27] However, their electrostatic capture still operates during non-sampling periods, thereby causing interference to the actual monitoring of bioaerosols. The piezoelectric effect has the unique ability to generate static electricity in response to mechanical stress. It can well solve the above problems by realizing the generation of self-powered static electricity for bioaerosol adsorption under capturing airflow disturbance only. $BaTiO_3$ (BTO), as a well-known remarkable charge storage and piezoelectric material, is frequently selected to provide a promising avenue for attracting and immobilizing charged airborne particles.[28−30]

To solve low interaction between virus and nanofibers, polydopamine (PDA), a bioinspired material derived from marine mussel adhesives, exhibits remarkable properties including strong adhesiveness, excellent underwater adhesion, and mild-condition self-polymerization.[31−34] Most of all, PDA has superior biocompatibility and can bind with biological molecules through electrostatic action and hydrogen and chemical bonds caused by active groups, including catechol group, phenolic hydroxyl group, amino group, aldehyde group, and 5,6-dihydroxyindole.[34−36] Tian et al.[37] find that a fiber membrane with PDA coating can effectively improve the filtration performance through the adhesion effect. Liu et al.[38] further demonstrate that nanofiber membranes coated based on the wet adhesion function of PDA have high-performance filtration in high-humidity environments. In addition, the adsorbed substances can be released under certain solvent and pH conditions.[39−41] Therefore, modified nanofibers to address particle adhesion, humidity adaptability, and inefficient elution challenges, the adhesive capture and controlled desorption performance of PDA modified nanofibers are promising candidates for application in the immobilization and elution of bioaerosols for subsequent quantitative analysis.

Herein, considering the challenges encountered in the accurate quantitative analysis of viral aerosols, we proposed a simple capture-analysis approach based on piezoelectric-electrostatic and bio-adhesive synergistic strategy to construct the electrostatic nanofibrous membrane to significantly enhance the capture and elution efficiency of viral aerosol. Considering the actual capturing requirements, polystyrene (PS) was chosen as the base polymer for its excellent electrospinnability, mechanical stability, and compatibility with BTO, besides its thermal/chemical stability. Furthermore, by combining with BTO piezoelectrics as an electret masterbatch and assembling a PDA viscous molecular layer, the $BaTiO_3$/PS/PDA (BPP) nanofibrous membrane was constructed with self-powered electrostatic and adhesive force to efficiently capture and elute airborne virus for quantitative analysis. The viral aerosol capture performance of the nanofibrous membrane at different flow velocities and atmospheric concentrations was further investigated. The comparison results of multiple commercial methods showed that the capture method based on a nanofibrous membrane was superior to that of the commercial ones. Our approach provides a promising pathway to developing viral aerosol capture for downstream quantification that surpasses traditional methods and can effectively address the challenges of viral aerosol monitoring.

2. EXPERIMENTAL SECTION

2.1. Fabrication of BPP Nanofibrous Membranes

The tetragonal $BaTiO_3$ nanoparticles (BTO NPs) powder of the defined fraction (1–10 wt %) was ultrasonically dispersed in a mixture solvent of dimethylformamide and tetrahydrofuran (mass ratio of 1:1). Afterward, the PS pellets were dissolved and magnetically stirred for 12 h at room temperature to prepare a homogeneous PS solution (15 wt %). All nanofiber membranes were fabricated using an ET-3556H spinning machine (Beijing Yongkang Leye Technology Development Co., LTD). Details of the materials, electrospinning process, and parameters are illustrated in Texts S1 and S2. The pristine PS nanofibers were prepared under the same electrospinning conditions for comparison. Further, by adjusting the distance and voltage of the electrospinning process, fiber membranes with different porosity distributions were also obtained. Specifically, increasing the needle-to-collector distance from 10 to 20 cm and decreasing the applied voltage from 20 to 12 kV resulted in progressively larger pore sizes and higher porosity (see detailed parameters in Table S1). Subsequently, the fibrous membrane was immersed in 60 mL of dopamine hydrochloride tris solution (0.50 mg mL^{-1}), and 5 mL of ammonia was added. After 12 h of reaction at room temperature, the product was washed twice with ultrapure water and absolute ethanol. Finally, the obtained membranes were dried at 35°C in a vacuum oven for 12 h to remove excess solvent and sealed for subsequent experimentation. The detailed preparation process of the BPP membrane is depicted in Figure 1a.

2.2. Materials Characterization

The detailed material characterization is illustrated in Text S3. Briefly, the crystalline structure was characterized by a Rigaku Ultima IV X-ray diffractometer (XRD, Japan Science and Technology Corporation). The surface morphology was characterized by a field-emission scanning electron microscope (Cryo-FESEM, SU8010). The surface element compositions were analyzed by an energy-dispersive spectrometer (EDS). Fourier transform infrared (FTIR) spectra were obtained by a Nicolet iS10 spectrometer (Thermo Scientific, USA). The specific surface areas and pore sizes were measured on an automatic volumetric sorption analyser (BELSORP-max, Micromeritics, Japan). The dispersion and morphology of BTO NPs in PS were characterized by a field transmission electron microscope (TEM, Talos F200S, FEI, Thermo Scientific) equipped with an energy-dispersive X-ray spectrometer (EDX). Surface potential and adhesion measurements were performed in an atomic force microscope (AFM, Dimension FastScan, Bruker),

https://doi.org/10.1021/acsami.6c09491
ACS Appl. Mater. Interfaces 2026, 18, 41004−41016

with sample preparation detailed in Text S4. Hydrophilicity of the membrane was characterized by a fully automatic contact angle measuring and contour analysis system (OCA100, Dataphysics). Zeta potential (ζ) was determined using a nanoparticle size and zeta potential analyzer (Zetasizer NANO ZS, Malvern).

The tensile tests were measured using an electronic universal testing machine (Inspekt Table Blue 5kN, Hegewald & Peschke, Germany). The porosity distribution was measured by mercury intrusion porosimetry (MicroActive AutoPore V 9600, Micromeritics Instrument Corporation, Norcross, GA, USA). The static voltage measurements (see Text S5 for details) were made using a Keithley 2400 digital source multimeter (Tektronix, Shanghai, China). The air pressure drops of the membranes were monitored by a digital differential pressure gauge during sampling with a flow velocity of 12.5 L min^{-1}. The piezoelectric coefficient (d_{33}) of BPP membranes was measured by a high-precision piezoelectric analyzer (PEAI1000, BALAB).

2.3. Batch Evaluation of Viral Aerosol Capture Performance

DNA phage T3 and RNA bacteriophage MS2 were used as model viral strains to evaluate the capture efficiency of BPP (see Text S6 for detailed preparation procedures). The capture performances for viral aerosol of the BPP membrane were determined using a self-customized bioaerosols generation and balancing system, which was described in our previous work.[36,42] The capture efficiency of the fibrous membrane was evaluated according to the GB/T 39990-2021 standard. Namely, the collection efficiency of the prepared filter membrane was calculated by comparing the collection scheme of the nanoaperture filter membrane with the filtration efficiency of the virus of more than 99.9% under the same conditions. Detailed information is provided in Text S7 and Figure S1.

The virus captured by the fibrous membrane was eluted by a mixture of tris and ascorbic acid (ASA) solution (pH = 4.5), followed by staining with the dye SYBR I. To quantify bacteriophage, after staining with SYBR I dye, visualization and counting were performed under a confocal microscope (LSM 800, Carl Zeiss) using a 100× oil mirror. The capture efficiency was calculated from the amount of virus in the BPP membrane elution relative to that of the reference filler. The determination of virus count was based on the reported methods.[43,44] Detailed determination of virus numbers and capture efficiency is provided in Texts S8 and S9.

2.4. Viral Aerosol Elution Assays for Quantification

To determine the optimal extraction conditions for subsequent virus quantification from the BPP membrane, the pH of the ASA and tris buffer elution solutions was optimized by measuring the elution yields from the BPP membrane. First, a known concentration of bacteriophage suspension was spiked onto BPP filters. Then, the membrane was freeze-dried and entered the elution process. The elution efficiency was calculated based on the eluted virus amount over the amount of virus originally spiked into the elution solution. Three independent elution experiments were performed for each of the porous membranes. Experimental details and calculation methods of elution efficiency are shown in Text S10.

2.5. Molecular Dynamics Simulation of Virus Adhesion and Elution

To validate the adhesive and elution results, molecular dynamics (MD) simulations were performed using the Gromacs 2021 software package with AMBER 99SB force fields to carry out 100 ns simulations. Due to the large molecular structure of protein and polymers, 1 repeat unit of the coated protein structure from the *Escherichia coli* bacteriophage MS2 (PDB ID: 2VTU, Figure S2), 3 PS, and 3 PDA structural units were used for subsequent simulation. The calculation details for protein-PS, protein-PDA, and protein-PDA-ASA complexes are described in Text S11.

2.6. Actual Application Performance Evaluation

To comprehensively evaluate the application of the filter membranes constructed for actual atmospheric environment monitoring, three commercial sampling methods were selected for comparison. These methods are the SKC biosampler (12.5 L min^{-1}, SKC Inc., Eighty Four, PA, USA), the Anderson six-stage cascade impactor (FA-1, 28.3 L min^{-1}, Applied Technical Institute of Liaoyang, China), and the large-flow cyclone biosampler (WL-4H, 350 L min^{-1}, BioCtech, China). To benchmark the field performance, the BPP was compared against conventional methods by measuring atmospheric virus concentrations simultaneously at the same location and sampling duration, with further evaluation across varying weather conditions. The BPP membrane was operated at its optimized flow rate of 15 L min^{-1} with a sampling time of 0.5 h. The sampling duration for each commercial sampler was kept consistent with that of the BPP membrane to ensure comparability. The capture efficiency followed the same procedure as detailed in Section 2.3 and Text S9. The on-site photo and meteorological parameters during actual sampling are listed in Figure S3 and Tables S2 and S3, respectively.

3. RESULTS AND DISCUSSIONS

3.1. Material Characterization of the BPP Nanofibrous Membrane

Figure 1a schematically illustrates the fabrication procedure of BPP nanofibrous membranes. A two-step process was employed to fabricate the self-powered fiber membranes, that is, BTO electrified PS fiber membranes were prepared through electrospinning technology, and self-assembled PDA molecular layers on their surfaces. The SEM image of the as-prepared BPP membrane exhibited a three-dimensional porous network structure composed of randomly oriented nanofibers (500 nm diameter) with uniformly distributed 40 nm BTO NPs embedded in the PS matrix (Figure 1b,c and Figures S4–S6). Further, combined EDS mapping of the BPP fibers confirms the homogeneous distribution of N and O elements across the fiber surfaces (Figure 1d), providing direct elemental evidence for the successful coating of a PDA active molecular layer. The TEM and EDX images of BPP showed a random distribution of BTO NPs in the PS fibers (Figure 1c and Figure S6). The homogeneous distribution of N across the fiber surface (Figure 1d and Figure S6) further confirmed the uniformity of the PDA layer. Since nitrogen is present exclusively in PDA, its EDX mass fraction of approximately 0.01% confirms an extremely low PDA loading (Table S4), corresponding to an ultrathin coating on the fiber surface. AFM characterization further showed that the fiber height increased by only about 2 nm after PDA deposition (Figures S4 and S7), providing direct evidence for the successful formation of a conformal yet extremely thin PDA layer. The molecular structures of chemically modified BPP nanofibers were further confirmed through FTIR spectra (Figure 1e). FTIR analysis revealed key vibrational modes in the samples. BTO showed characteristic stretching vibrations at ~610 (TiO_6 octahedron), ~1420/1643 (Ba–Ti–O bonds), and 3447 cm^{-1} (hydroxyl stretching). In PS/BTO composites, the weakened 3453 cm^{-1} peak further confirmed hydroxyl presence, while other peaks correspond to PS vibrations (e.g., aromatic C–H stretches at 3062/3028 cm^{-1}, ring modes at 1602/1496/1449 cm^{-1}). After PDA coating, new stretches emerged at 3351 (O–H) and 3285 cm^{-1} (C–N), along with phenolic C–O–H/C–N–H vibrations (1395/1345/1212 cm^{-1}),[45] further confirming successful PDA coating.

https://doi.org/10.1021/acsami.6c09491
ACS Appl. Mater. Interfaces 2026, 18, 41004−41016

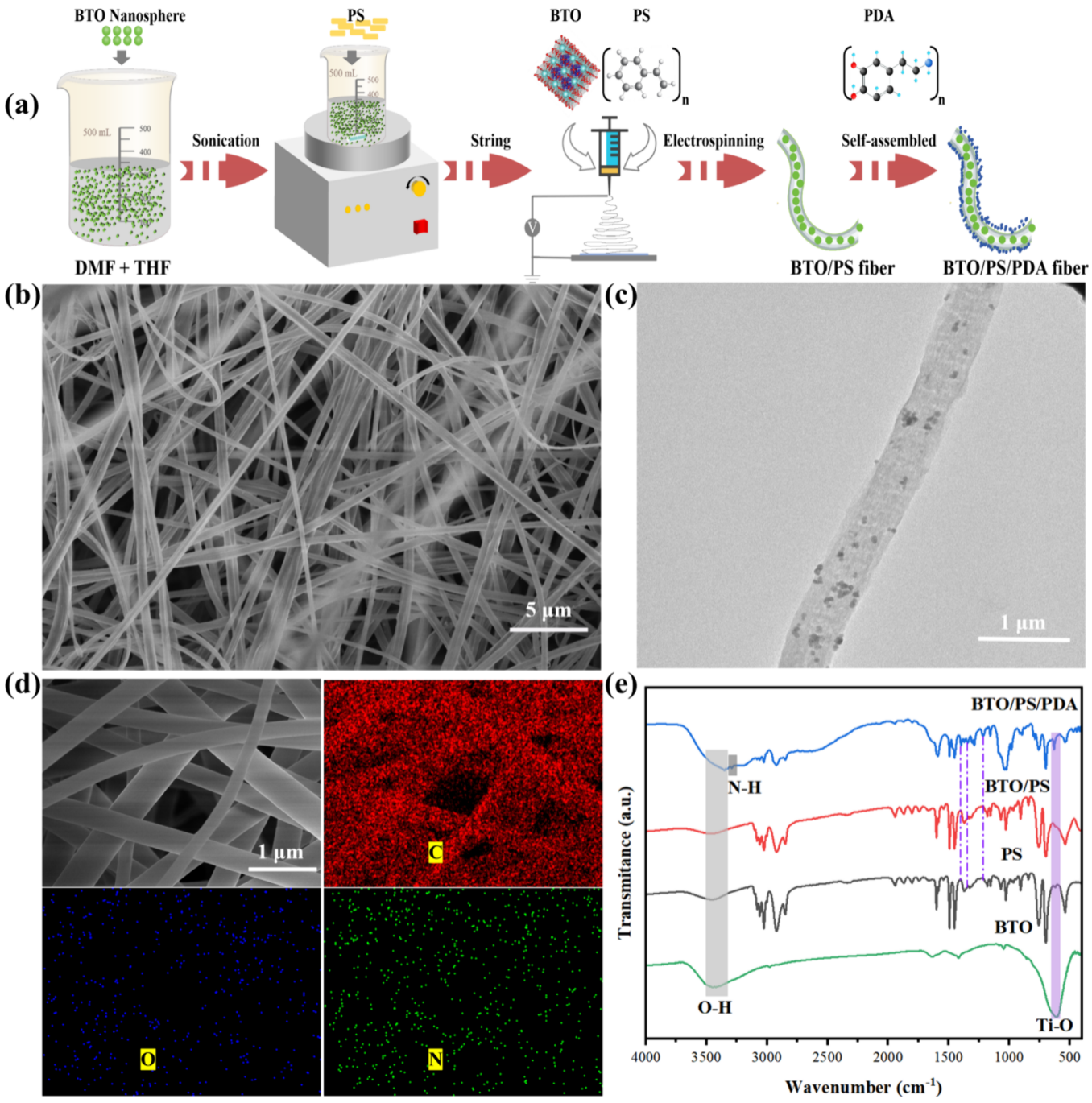

Figure 1. Fabrication and characterization of the nanofibrous BPP. (a) Schematic illustration for fabrication of BPP nanofiber membranes; (b) SEM and (c) TEM images of BPP nanofiber; (d) EDS mapping of C, N, and O elements on the surface of BPP; (e) FTIR patterns of BTO NPs and PS, BTO/PS, and BPP nanofibrous membranes.

The crystal structure and surface characteristics of the as-prepared membranes were verified using XRD and BET surface area analysis. All the XRD patterns appeared to be a broadly-shaped peak visible at approximately $2\theta = 20°$ due to the PS (Figure S8). On this basis, the diffraction peaks of prepared BTO/PS were attributed to the tetragonal phase of BTO (JCPDS, No. 05-0626). XRD revealed the preserved tetragonal BTO crystal structure within the amorphous PS matrix. Meanwhile, BET results revealed that the specific surface area of BPP nanofibers is 287.64 $m^2\ g^{-1}$, indicating that the obtained BPP membrane possesses a high specific surface area (Figure S9). These results collectively demonstrated successful fabrication of a structurally intact, functionally integrated composite membrane.

3.2. Viral Aerosol Capture Performance of the BPP Nanofibrous Membrane

A filtration-based capture method was established to effectively collect the full spectrum of viral aerosols, including small free virus suspended individually in the atmosphere and viral particles attached to larger atmospheric particulate matter that are

https://doi.org/10.1021/acsami.6c09491
ACS Appl. Mater. Interfaces 2026, 18, 41004−41016

prone to transfer loss. Using this method, the viral aerosol capture performance of the BPP nanofibrous membrane was evaluated by using MS2 of single-stranded RNA and T3 of double-stranded DNA bacteriophages as model viruses. The diameters of MS2 and T3 are about 27 and 47 nm, respectively.[4,11,16] After aerosolization, the aerodynamic diameter is mainly distributed in the range of 0.3–0.5 μm (Figure S10). The following experiments were evaluated with a BPP nanofibrous membrane with a porosity of 965 nm (Figure S11).

As Figure 2a shows, the BPP nanofibrous membrane exhibited significantly enhanced capture efficiencies to 95.3% and 97.2% for MS2 and T3, respectively, representing an approximately three-fold increase over the pure PS membrane with PDA modification (30% and 35%). SEM images confirmed that viral aerosol was captured onto the surface of the BPP nanofiber (Figure S12). At a mass concentration of 7% BTO addition, the static voltage of the nanofiber membrane reaches a maximum of ∼2 V among all samples (Figure 2b), corresponding to the superior capture efficiency. Therefore, 7 wt % BTO loading was chosen as an optimal value for further experiments. SEM imaging across BTO loadings (0–9 wt %) confirmed uniform fiber morphology without detectable aggregation or bead formation (Figure S13). This rules out morphological degradation as a cause for the performance decline above 7 wt % BTO.

Additionally, the capture efficiency of viral aerosol by the nanofibrous membrane at different sampling flow rates was investigated. As Figure 2c shows, at flow velocity up to 15 L min^{-1}, the capture efficiency of the membrane for MS2 and T3 reached about 95%. In fact, due to the fine size of the fiber filaments, the static voltage generated by deformation under different flow rates is almost the same (Figure S14). However, the capture performance of nanofibrous membranes was gradually decreased as the flow velocity exceeded 15 L min^{-1}. This may be due to the reduced contact time between viral particles and the nanofibrous membranes at higher flow velocity, and the adhesion force on the nanofiber surface to the virus particles cannot resist the high flow rate, resulting in the virus particles being blown away by the airflow.

Apart from mass concentration of BTO addition and sampling velocity, the influence of atmospheric concentration and relative humidity (RH) on viral aerosol capture efficiency of the BPP nanofibrous membranes was also investigated. When RHs of the balance chamber ranged (40%–90%) ± 5%, which encompasses most common atmospheric conditions, the capturing efficiency of BPP nanofibrous membranes reached 92.3%–98.3% (Figure 2d). The result showed that the nanofibrous membrane maintained a stable capture efficiency across a wide RH range, demonstrating the method's practical applicability in diverse environments. As Figure S15 shows, the membranes exhibit a hydrophobic surface with contact angles of 115°, indicating that it has strong moisture resistance. A hydrophobic surface hinders the formation of hydrogen bonds with water molecules, thereby impeding the adherence of water molecules to the nanofibrous surface.[46,47] In addition, no distinct degradation in capture efficiency is also found under different atmospheric concentrations and

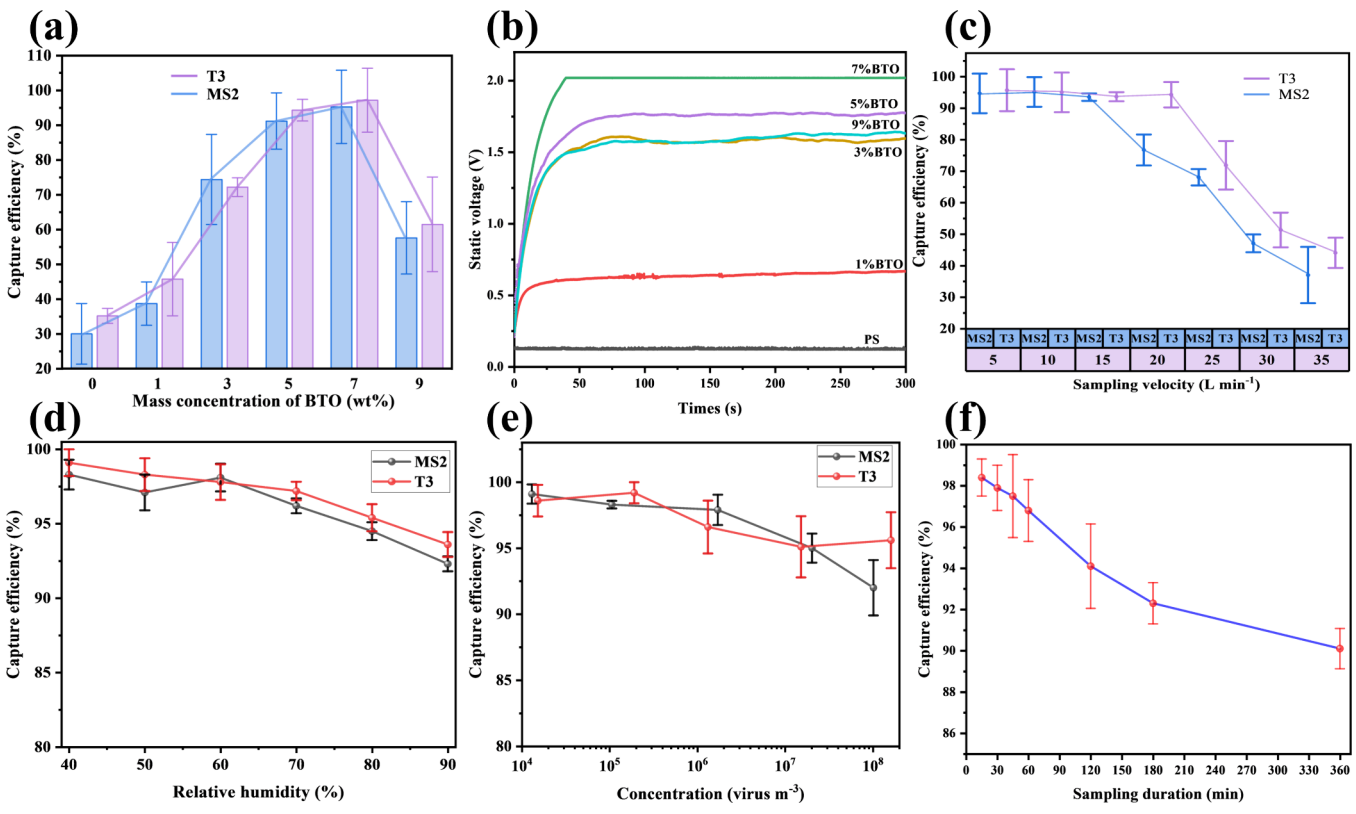

Figure 2. Viral aerosol capture performance and environmental adaptability of the BPP membranes. (a) Capture efficiency of bioaerosol by BPP nanofibrous membranes with different BTO ratios (0, 3, 5, 7, and 10 wt %). Note: The BTO concentration of 0 corresponds to the pure PS membrane with PDA modification. (b) Static voltage curves of different BPP nanofibrous membranes; (c) capture efficiency at different flow velocities; (d–f) capture efficiency of BPP under different atmospheric RHs, atmospheric concentrations, and sampling durations.

https://doi.org/10.1021/acsami.6c09491
ACS Appl. Mater. Interfaces 2026, 18, 41004–41016

sampling duration up to 6 h (Figure 2e,f). Even at an atmospheric concentration of 10^8 virus m^{-3} and a sampling time of 360 min, the capture efficiency remained above 90%. These results indicate that the BPP nanofibrous membranes really have an excellent capture stability for viral aerosol under high RH and a continuous sampling system for long periods. All these findings support the considerable potential of the nanofibrous membrane for efficient collection of viral aerosol due to its good environmental adaptability.

3.3. Elution Performance and Practical Application of BPP Nanofibrous Membrane

To achieve accurate downstream quantitative analysis, efficient elution of captured viral aerosols is also very crucial from adhesive nanofibers. PDA, well known for its bioaffinity, requires optimized elution conditions to release adsorbed biomolecules for quantification. It was pointed out that the elution of substances adsorbed by PDA is affected by the solvent type, oxidation-reduction substance, and pH.[48−50] To minimize nucleic acid damage, a mild elution method was established with ASA added into the Tris buffer (10 mM) as eluent. ASA acts as an antioxidant and has excellent free radical scavenging ability to reduce the damage of genetic acids against oxidative stress.[51,52] Meanwhile, it also acts as a pH adjustment, weakening the electrostatic attraction between PDA and microorganisms.

The elution effects of specific pH gradient elution conditions are performed (Figure 3a). Systematic evaluation of pH between 4.5 and 9.5 revealed that elution efficiency increased at lower pH, optimal (>98%) at pH < 6.5. The elution effect with different pH values was further verified using SEM and fluorescence microscopy. The fiber and phage mixture was stained with fluorescent dye, and the image of fluorescence microscopy in Figure 3b shows that there was no attachment of virus particles onto the surface of the nanofiber after elution under a pH value lower than 6.5. The SEM images also revealed that almost no virus particles were attached onto the nanofibers

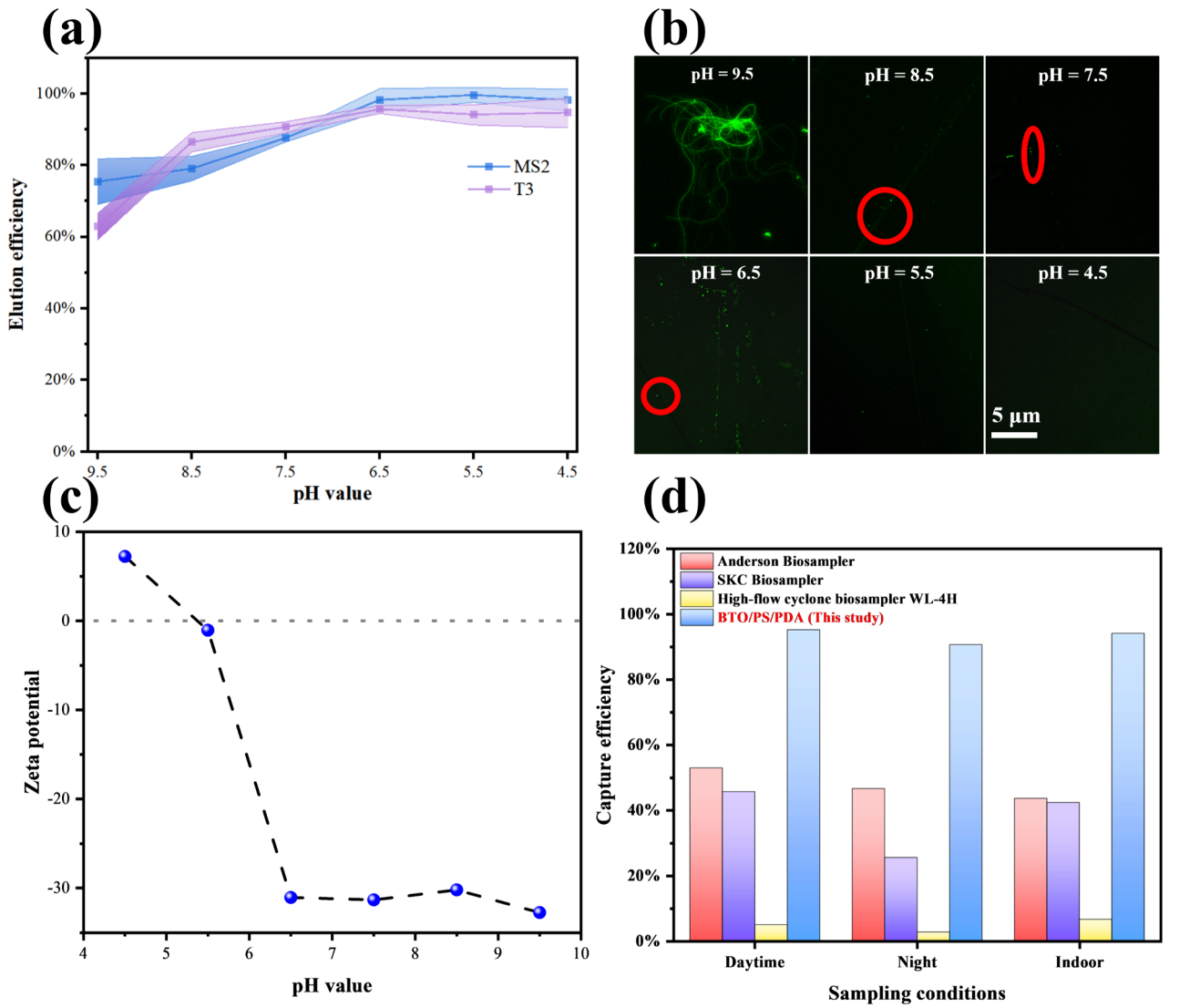

Figure 3. Elution performance and practical application potential of the nanofibrous BPP membrane. (a) Elution efficiency of tris/ASA eluates at different pHs on BPP nanofibrous membranes with captured bioaerosol; (b) fluorescence image of phage and fiber after elution with different pHs; (c) ζ potential of BPP nanofibrous membranes as a function of elute pH value; (d) comparison of viral aerosol concentration evaluated by BPP nanofibrous membranes with commercial methods.

https://doi.org/10.1021/acsami.6c09491
ACS Appl. Mater. Interfaces 2026, 18, 41004−41016

in the desorbed samples under these conditions of pH < 6.5 (Figure S12). To investigate the reasons for this pH-induced elution effect, the nanofibers under elution of different pH values were characterized using zeta potential. As Figure 3c shows, when the pH value of the elution system exceeds 6.5, the surfaces of the BPP nanofibrous membranes become negatively charged, leading to an increase in electrostatic repulsion between PDA and virus. Thereby making it easier to elute virus particles from the surface of BPP nanofibrous membranes. Furthermore, this study characterized the adhesive force of nanofibers under eluents of different pH values using AFM. After being treated by the eluent, the surface adhesion force of BPP nanofiber exhibits a remarkably decreased trend with the eluent pH value, thus exhibiting good elution performance against the captured virus (Figure S16). Therefore, the elution ability of the low-pH eluent may be due to its combined effect on the electrostatic interactions and adhesion forces of the BPP nanofibers. To further evaluate the operational durability of the BPP membrane for practical environmental monitoring, we performed repeated capture-elution-drying cycles using the same BPP membrane. As Figure S17 shows, the capture efficiency remained above 90% during the first two cycles but dropped significantly in subsequent cycles. The static voltage of the membrane also showed a gradual decrease with increasing cycle number, indicating that the piezoelectric output of the BTO/PS fibers deteriorates with repeated use. Therefore, for field applications requiring continuous monitoring, we recommend using fresh membranes for each sampling event to ensure optimal and reliable capture efficiency. This limitation also points to future directions for improving membrane durability, such as reinforcing the mechanical stability of the piezoelectric network or developing more robust coating strategies. Therefore, the method based on BPP fibrous membranes provides a better solution for accurately simulating the presence of viruses in the atmosphere.

To comprehensively evaluate the application of the constructed BPP nanofibrous membranes for actual atmospheric environment monitoring, three commercial sampling methods were selected for comparison. To ensure the accuracy of the comparative experiment, different times and locations were also tested. As classical bioaerosol samplers, the SKC biosampler, the six-stage Anderson biosampler, and the high-flow cyclone biosampler (Type: WL-4H) are widely used in the collection and research of bioaerosols. It should be noted that each commercial sampler was operated at its manufacturer-recommended optimal flow rate (SKC: 12.5, Anderson: 28.3, Cyclone: 350 L min^{-1}), while the BPP membrane was operated at its optimized flow rate of 15 L min^{-1}. To account for differences in sampling volume, the comparison in Figure 3d is based on relative capture efficiency calculated using a nanoscale filtration membrane (near 100% capture efficiency) as the reference standard. The BPP membrane clearly exhibits superior capture efficiency compared to the commercial samplers.

As displayed in Figure 3d, our actual observational data indicate that the above three sampling methods have extremely lower concentration assessments than the BPP nanofiber method. The result indicates that the BPP nanofiber membrane exhibits superior capture efficiency. In addition, under different weather conditions, the atmospheric concentrations of viral aerosol evaluated by the BPP nanofiber method were 1.7–2.2 times that of the Anderson sampler, 2.0–3.5 times that of SKC, and 14.1–33.8 times that of the large-flow cyclone sampler (Figure 3d). The above results further indicate that the fibrous membrane constructed in this study is more reliable for collecting viral aerosols compared to the conventional biological aerosol sampling methods. Conversely, the results also showed that these classical samplers have relatively low capture efficiency for viral aerosols. It is consistent with what the relevant studies have pointed out that SKC and cyclone samplers are inadequate in collecting submicrometric and ultrafine virus particles, since the physical collection efficiency for viral aerosol is less than 20%.[11,15] For instance, Li et al.[15] find that SKC BioSampler recovers only up to 5% of influenza virus particles, while the gelatin filter achieves at most 1.5%, and the glass fiber filter shows negligible virus recovery. Similarly, the Anderson six-stage sampler has also been proven to have an overall biological collection efficiency of only 0.25%.[13] Furthermore, relevant studies have reported that long-term sampling (e.g., 60 min) can substantially reduce the efficiency of liquid-based biosamplers (e.g., cyclone and impinger types) due to liquid splashing and re-aerosolization.[53] In contrast, our BPP membrane maintains >90% capture efficiency even under prolonged sampling conditions and high-humidity environments, demonstrating a substantial improvement over existing commercial samplers. Therefore, the method based on BPP fibrous membranes provides a better solution for accurately simulating the presence of viruses in the atmosphere.

3.4. Capturing Mechanisms of Viral Bioaerosol

Depending on the above-mentioned discussions of Section 2.2, by roughly comparing the capture performance differences between nanofibrous membranes containing different BTO additions and pure PS fiber, as well as the electrostatic voltage variations under different BTO ratios, the role of electrostatic force can be roughly inferred. As Figure 4a shows, Kelvin probe force microscopy (KPFM) measurements confirmed that bending deformation significantly increased the surface potential of the BPP nanofiber from an average of 5.75 to 6.5 V. To further confirm that the observed static voltage originates from the piezoelectric effect of BTO rather than a remnant charge from electrospinning process, we compared the voltage output of the BPP membrane vs a pure PS control under static conditions (without airflow) and under active airflow stimulation. As Figure S18 shows, the results demonstrated that the BPP membrane generated a stable and reproducible voltage upon airflow stimulation, whereas the PS control and BPP without airflow showed a negligible response. This confirms that the voltage is dynamically generated by the piezoelectric BTO NPs under mechanical deformation, rather than being a residual charge from the electrospinning process. It was noted that, by increasing the doping ratio of BTO from 1% to 9%, the capturing efficiency of viral particles increases first and then decreases (Figure 2a), which is consistent with the variation of electrostatic voltage caused by the elastic modulus change of nanofibers (Figure 2b, Figure S19, and Table S5). Notably, the piezoelectric coefficient (d_{33}) of the composite membranes increased monotonically with higher BTO content (Figure S20), suggesting that the intrinsic piezoelectric activity of the material alone does not explain the observed optimum at 7 wt %. Instead, we attribute the decline in performance beyond 7 wt % to the reduced elastic modulus of the composite fibers at higher BTO loadings. A lower elastic modulus diminishes the mechanical stress transferred to the embedded BTO NPs under airflow, thereby weakening the piezoelectric response and the resulting electrostatic capture

https://doi.org/10.1021/acsami.6c09491
ACS Appl. Mater. Interfaces 2026, 18, 41004–41016

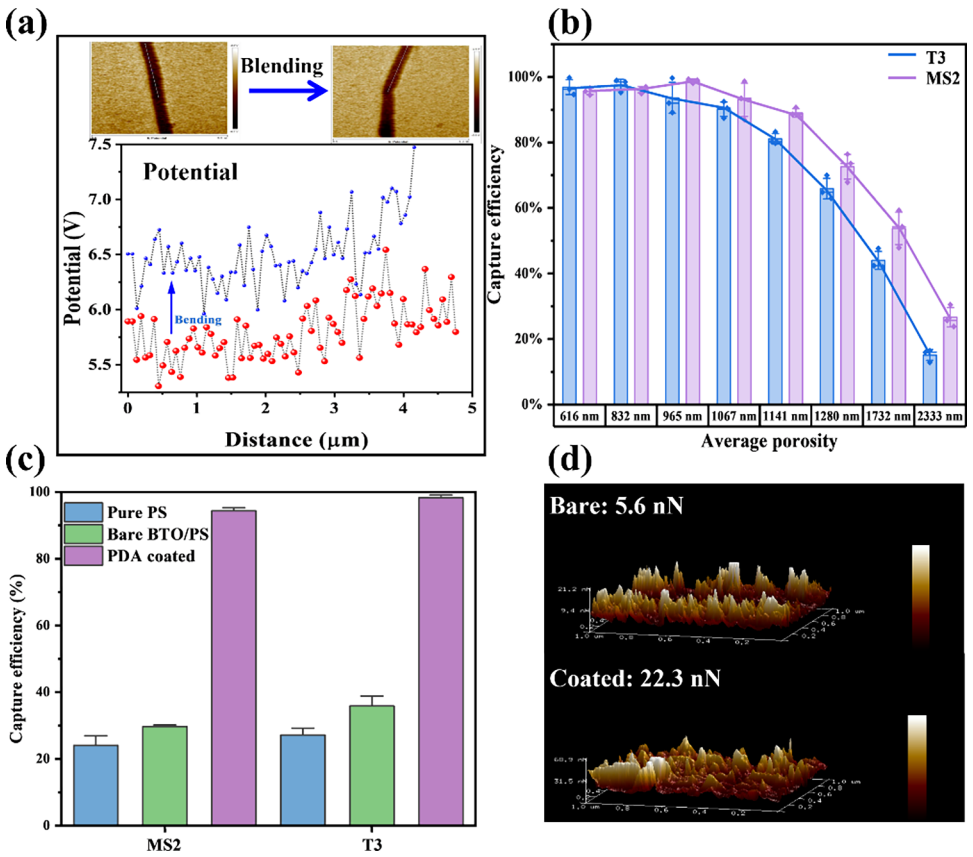

Figure 4. Physical mechanism of static-chemo-synergistic bioaerosol capture. (a) KPFM mapping of surface potential of BPP nanofibrous membranes before and after bending deformation; (b) capture efficiencies of BPP nanofibrous membranes as a function of porosity. (c) Comparisons of bioaerosol capture efficiencies of the pure PS, with and without PDA coating membranes. (d) Adhesive forces of fibers with and without PDA modification.

efficiency. This interpretation was further supported by the stress-strain curves (Figure S19) and corresponding elastic modulus data (Table S5), collectively indicating that the mechanical deformability of the fibers plays a critical role in modulating piezoelectric output. Therefore, the optimal capture performance at 7 wt % BTO represented a balance between sufficient piezoelectric charge generation and adequate mechanical stiffness, rather than a simple function of BTO content alone.

To further reveal the role of electrostatics, the porosity of the membranes was systematically adjusted to modulate their electric field distribution. As Figure 4b shows, by adjusting the porosity of BPP nanofibrous membranes to regulate the distribution of the electrostatic field, it was found that a smaller porosity leads to a higher capture efficiency. Lower porosity, indicative of denser fiber packing, resulted in a more concentrated electrostatic field.[54] In fact, the results show that the pressure drop gradually increases as the porosity decreases (Figure S21). These findings suggest that an optimal pore size of ∼965 nm, together with 7 wt % BTO doping and PDA coating, represents a balanced design that maximizes capture efficiency while minimizing pressure drop. Given that the pore sizes of BPP nanofibrous membranes were significantly larger than the viral particles, physical interception was deemed negligible in this study.[25,55] Therefore, we speculate that the main function of staticelectric is mainly to attract charged virus particles, and higher staticelectric is conducive to drawing airborne virus away from the airflow and towards the surface of the fiber filaments.

To illustrate the role of PDA in viral aerosol capture, a comparison of the capture efficiency between bare and PDA-coated nanofibers was also conducted. As Figure 4c shows, pure PS and bare BTO/PS of 965 nm porosity with nearly low efficiency (∼30%) for MS2 and T3. By coating PDA onto the surface of the nanofiber, the capturing efficiency of BTO/PA/PDA increased to 95.8% for MS2 and 97.2% for T3, respectively. Therefore, without the adhesion provided by PDA, captured viruses are easily blown away by the airflow. The humidity-dependent capture efficiency of bare BTO/PS membranes further supports this conclusion. As Figure S22 shows, higher RH substantially reduces the capture efficiency of bare BTO/PS membranes (∼6%–35%), highlighting the critical role of PDA adhesion in maintaining high performance and even under moist conditions. Actually, the surface adhesive force of the bare BTO/PS and the BPP nanofibrous membranes was also measured with AFM (Figure 4d). Comparing fibrous membranes with and without PDA coating. PDA coating can significantly increase the adhesion of the nanofibrous membrane. The adhesive force of the nanofiber increased from 5.6 to 22.3 nN when PDA was anchored onto BTO/PS nanofibers.

It is worth clarifying that the thin molecular layer of PDA coating does not alter the piezoelectric response of the underlying BTO/PS fibers. As confirmed by the piezoelectric output measurements, the BTO/PS fibers and the PDA-

https://doi.org/10.1021/acsami.6c09491
ACS Appl. Mater. Interfaces 2026, 18, 41004–41016

coated BPP membranes exhibited nearly identical voltage outputs under identical mechanical stimulation (Figure S18), indicating that the PDA layer does not interfere with the charge generation capability of the embedded BTO NPs. Operating independently yet synergistically, piezoelectricity provides physical attraction to draw viral particles toward the fiber surface, while PDA exerts chemical anchoring to retain them. Comparing the PDA-coated BPP membrane with the bare BTO/PS membrane under varying humidity conditions (Figure 2d and Figure S22), the BPP membrane consistently exhibits substantially higher capture efficiency than the bare BTO/PS membrane across all humidity conditions. The presence of PDA consistently leads to substantially higher capture efficiency, particularly at high humidity, where electrostatic attraction alone is largely diminished. Thus, the electrostatic field facilitates initial physical capture, but subsequent retention critically depends on PDA-mediated chemical adhesion.

To better understand the experimental results, MD simulations were also performed to compare the interaction energies of different surfaces and to examine the functional groups of the interaction. Comparatively, the total interaction energies of the outer capsids of MS2 with two different surfaces, PS

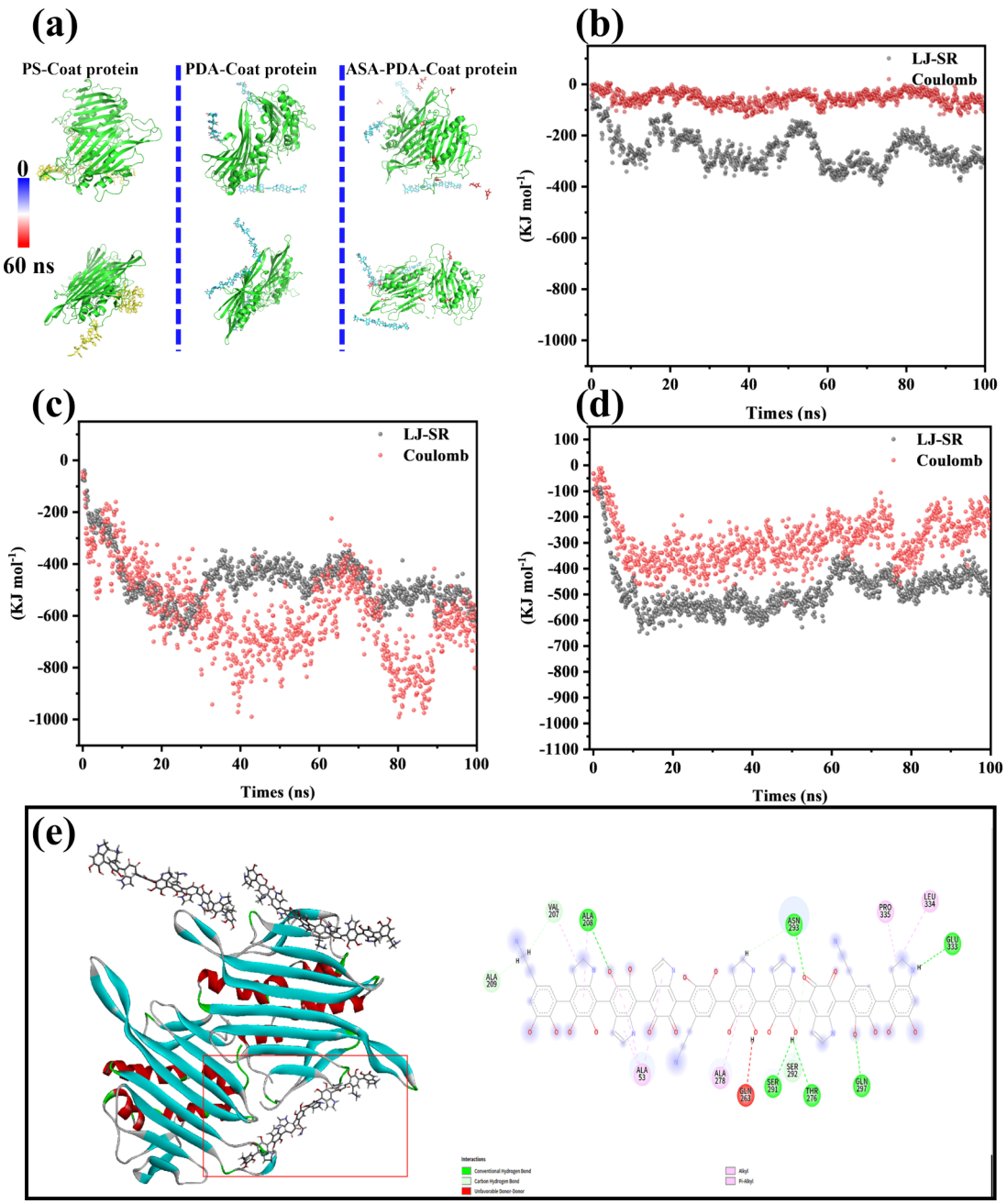

Figure 5. Chemical adhesion molecular mechanism for capturing bioaerosol. (a) MD snapshot analysis of interactions between the MS2 viral capsid protein and PS, PDA, as well as the interaction of capsid proteins adsorbed on the PDA surface in ASA solution; (b, c) PS and PDA interaction energies with proteins; (d) interaction energy of PDA with coated proteins under ASA treatment conditions; (e) MD simulations of 100 ns for the interaction between PDA and coated protein.

https://doi.org/10.1021/acsami.6c09491
ACS Appl. Mater. Interfaces 2026, 18, 41004−41016

and PDA, were calculated by MD simulation to be −311.70 and −1062.69 kJ·mol^{-1}, respectively (Figure 5b–d and Table S6). The simulation snapshots showed that viral aerosols adhere to the PS surface mainly by forming amide–π stacks and π–alkyl bonds with amino acid residues of the outer capsid protein of virus particles (Figure S23). However, PDA can not only form amide-π stacking interaction and π–alkyl bonds with the capsid protein through the benzene ring in the molecular structure, but also produce a series of forces (electrostatic attraction, hydrogen bonding, unfavorable donor–donor interaction, etc.) with the hydroxyl group, carboxyl group, and amino group on the capsid protein of virus (Figure 5e). Specifically, conventional hydrogen bonds are formed with the following amino acid residues: alanine (ALA) 208, asparagine (ASN) 293, glutamic acid (GLU) 333, glutamine (GLN) 297, threonine (THR) 276, and serine (SER) 291. Carbon–hydrogen bonds are observed with alanine (ALA) 209, valine (VAL) 207, and serine (SER) 292. An unfavorable donor-donor interaction is identified with glutamine (GLN) 263. Alkyl interactions are formed with alanine (ALA) 53, alanine (ALA) 278, proline (PRO) 335, and leucine (LEU) 334. In addition, π–alkyl interactions are also observed with further residues, as illustrated in Figure 5e. A lower interaction energy indicates a higher binding affinity. The theoretical calculation results further proved that the PDA coating could significantly enhance its binding force to virus particles, making it difficult to be blown away by airflow and thus affecting its capture performance for viral aerosol.

In situ FTIR results of Figure S24 showed that the characteristic peaks of functional groups, such as the amino group and hydroxyl group of BPP nanofibrous membranes, disappeared after capturing the virus particles. It further confirmed that the surface of PDA modification was bound to viral surface proteins. Therefore, once a viral particle attaches to the surface of nanofibers, the virus will be immobilized by PDA to prevent it from being blown away by the airflow. Thus, these multiple interactions enhance the immobilization ability of the nanofiber surface to the virus, thereby benefiting the capture efficiency. The substantial efficiency gap between PDA-coated and uncoated membranes underscores the importance of adhesive forces in the capture process. It further indicates that an efficient virus aerosol capture efficiency can be achieved based on the underlying mechanism of electrostatic adsorption and chemical adhesion.

For subsequent virus quantification, the results indicated that the mild desorption method based on ascorbic acid has a better desorption efficiency for BPP nanofibrous membranes. The theoretical calculation results also demonstrated that the addition of ascorbic acid can significantly affect its interaction energy under weakly acidic conditions (Figure S23 and Table S6), with only tyrosine (TYR) 386 and ASN 412 residues remaining as interaction sites. Therefore, captured viruses are eluted by mechanical shaking in ASA/Tris solution. This was also confirmed from the FTIR spectra of the eluted BPP nanofibrous membranes, which exhibit the two small peaks of the amino and hydroxyl groups disappeared (Figure S25). Notably, the elution efficiency exhibited a strong pH dependence (Figure 3a), with acidic and weakly acidic conditions yielding substantially higher elution efficiency. This experimental trend was fully consistent with the theoretical MD calculations (Table S7), showing that the binding energy between PDA and viral capsid proteins decreases progressively with lowering pH. Lower binding energy under acidic conditions facilitates virus detachment, in full agreement with the observed pH-dependent elution behavior. Therefore, under weakly acidic conditions, the virus particles captured onto the PDA surface could easily fall off under the shaking of the eluate. The excellent agreement between experiment and theory confirms that ascorbic acid-assisted elution at mildly acidic pH provides an efficient and gentle means for the virus to be eluted from the BPP membrane, while preserving viral integrity for downstream quantitative analysis.

4. CONCLUSIONS

In this study, a static-chemo-synergistic bioaerosol capture approach based on a nanofiber membrane has been successfully developed for electrostatic attraction and adhesive capturing of viral aerosol. The results confirmed the important role of electrostatic forces in conjunction with surface adhesion forces for viral aerosol capturing. The viral aerosol capture efficiency of the prepared nanofibrous membrane was achieved above 95% at a high flow rate. It provides excellent environmental adaptability for viral aerosol capturing at long duration, high flow rate, and relative humidity. The mechanism by which this nanofiber membrane efficiently captures viral aerosols mainly consists of two aspects: one is the self-powered electrostatic force from stress-induced piezoelectric effect of BTO NPs resulting from the deformation of PS, and the other is the adhesion effect of polydopamine onto the surface of the nanofiber membrane. The synergy of the above two has significantly enhanced the capture efficiency of viral aerosols. Moreover, by manipulating the pH of the eluate with ascorbic acid and performing a comparative analysis of nanofibrous membranes with different chemical structures, a mild mode of desorption was also developed for further quantification. The present result provides a theoretical insight into the design of viral aerosol capturing technology with high efficiency and easy desorption properties for subsequent quantification.

■ ASSOCIATED CONTENT

Supporting Information

The Supporting Information is available free of charge at https://pubs.acs.org/doi/10.1021/acsami.6c09491.

AFM height image of the BPP fiber; SEM image of the $BaTiO_3$ nanoparticles; TEM and EDX mapping images of the BTO/PS fibers; XRD patterns; nitrogen adsorption–desorption isotherm curves of the BPP membrane; aerodynamic diameter distribution of generated MS2 and T3 viral aerosols; porosity regulation results of the BPP fibrous membranes; SEM images of the BPP membrane before and after elution; electrostatic voltage of the 7% BPP membrane under different flow velocities; water contact angles demonstrating the hydrophobic properties of BTO/PS and BPP; adhesive force variation of the BTO/PS/PDA fibers treated by different elution solutions of pH value; stress–strain curves of BTO/PS fibrous membrane samples; comparison of pressure drops across BPP membranes with different porosities; capture efficiency of bare BTO/PS under different atmospheric RHs; structure of the MS2 capsid protein (PDB ID: 2VTU); MD simulation snapshots (100 ns) of PS-

https://doi.org/10.1021/acsami.6c09491
ACS Appl. Mater. Interfaces 2026, 18, 41004−41016

and PDA-capsid interactions; FTIR of the BPP membrane after virus capture and elution; schematic diagram of the experimental setup for evaluating membrane capture performance; and photographs of field sampling under ambient atmospheric conditions and pre-treated BPP membranes (DOCX)

AUTHOR INFORMATION

Corresponding Author

Taicheng An – *Guangdong-Hong Kong-Macao Joint Laboratory for Contaminants Exposure and Health, Guangdong Key Laboratory of Environmental Catalysis and Health Risk Control, Institute of Environmental Health and Pollution Control, Guangdong University of Technology, Guangzhou 510006, China; Guangdong Basic Research Center of Excellence for Ecological Security and Green Development, Guangdong Technology Research Center for Photocatalytic Technology Integration and Equipment Engineering, School of Environmental Science and Engineering, Guangdong University of Technology, Guangzhou 510006, China;* orcid.org/0000-0001-6918-8070; Email: antc99@gdut.edu.cn

Authors

Feihong Xue – *Guangdong-Hong Kong-Macao Joint Laboratory for Contaminants Exposure and Health, Guangdong Key Laboratory of Environmental Catalysis and Health Risk Control, Institute of Environmental Health and Pollution Control, Guangdong University of Technology, Guangzhou 510006, China; Guangdong Basic Research Center of Excellence for Ecological Security and Green Development, Guangdong Technology Research Center for Photocatalytic Technology Integration and Equipment Engineering, School of Environmental Science and Engineering, Guangdong University of Technology, Guangzhou 510006, China*

Guiying Li – *Guangdong-Hong Kong-Macao Joint Laboratory for Contaminants Exposure and Health, Guangdong Key Laboratory of Environmental Catalysis and Health Risk Control, Institute of Environmental Health and Pollution Control, Guangdong University of Technology, Guangzhou 510006, China; Guangdong Basic Research Center of Excellence for Ecological Security and Green Development, Guangdong Technology Research Center for Photocatalytic Technology Integration and Equipment Engineering, School of Environmental Science and Engineering, Guangdong University of Technology, Guangzhou 510006, China;* orcid.org/0000-0002-6777-4786

Linghui Peng – *Guangdong-Hong Kong-Macao Joint Laboratory for Contaminants Exposure and Health, Guangdong Key Laboratory of Environmental Catalysis and Health Risk Control, Institute of Environmental Health and Pollution Control, Guangdong University of Technology, Guangzhou 510006, China; Guangdong Basic Research Center of Excellence for Ecological Security and Green Development, Guangdong Technology Research Center for Photocatalytic Technology Integration and Equipment Engineering, School of Environmental Science and Engineering, Guangdong University of Technology, Guangzhou 510006, China*

Jianhua Qi – *Key Laboratory of Marine Environment and Ecology, Ministry of Education, Ocean University of China, College of Environmental Science and Engineering, Ocean University of China, Qingdao 266100, China;* orcid.org/0000-0002-3800-239X

Zhishu Liang – *Guangdong-Hong Kong-Macao Joint Laboratory for Contaminants Exposure and Health, Guangdong Key Laboratory of Environmental Catalysis and Health Risk Control, Institute of Environmental Health and Pollution Control, Guangdong University of Technology, Guangzhou 510006, China; Guangdong Basic Research Center of Excellence for Ecological Security and Green Development, Guangdong Technology Research Center for Photocatalytic Technology Integration and Equipment Engineering, School of Environmental Science and Engineering, Guangdong University of Technology, Guangzhou 510006, China;* orcid.org/0009-0006-2048-514X

Jiani Wang – *Guangdong-Hong Kong-Macao Joint Laboratory for Contaminants Exposure and Health, Guangdong Key Laboratory of Environmental Catalysis and Health Risk Control, Institute of Environmental Health and Pollution Control, Guangdong University of Technology, Guangzhou 510006, China; Guangdong Basic Research Center of Excellence for Ecological Security and Green Development, Guangdong Technology Research Center for Photocatalytic Technology Integration and Equipment Engineering, School of Environmental Science and Engineering, Guangdong University of Technology, Guangzhou 510006, China*

Simeng Zhang – *Guangdong-Hong Kong-Macao Joint Laboratory for Contaminants Exposure and Health, Guangdong Key Laboratory of Environmental Catalysis and Health Risk Control, Institute of Environmental Health and Pollution Control, Guangdong University of Technology, Guangzhou 510006, China; Guangdong Basic Research Center of Excellence for Ecological Security and Green Development, Guangdong Technology Research Center for Photocatalytic Technology Integration and Equipment Engineering, School of Environmental Science and Engineering, Guangdong University of Technology, Guangzhou 510006, China*

Huijun Zhao – *Guangdong-Hong Kong-Macao Joint Laboratory for Contaminants Exposure and Health, Guangdong Key Laboratory of Environmental Catalysis and Health Risk Control, Institute of Environmental Health and Pollution Control, Guangdong University of Technology, Guangzhou 510006, China; Guangdong Basic Research Center of Excellence for Ecological Security and Green Development, Guangdong Technology Research Center for Photocatalytic Technology Integration and Equipment Engineering, School of Environmental Science and Engineering, Guangdong University of Technology, Guangzhou 510006, China;* orcid.org/0000-0002-3028-0459

Complete contact information is available at: https://pubs.acs.org/doi/10.1021/acsami.6c09491

Author Contributions

F.X. conceived the idea, conducted experiments and tests, writing original draft. G.L., L.P., J.Q., and Z.L. reviewed and edited the paper. J.W. and S.Z. assisted with the experiments and data analysis. H.Z. supervised this project. T.A. supervised this

https://doi.org/10.1021/acsami.6c09491
ACS Appl. Mater. Interfaces 2026, 18, 41004−41016

project and conceived the idea. All authors contributed to the discussions and commented on the paper.

Notes

The authors declare no competing financial interest.

■ ACKNOWLEDGMENTS

This work was supported by the National Natural Science Foundation of China (U25A20814 and 42407510), Introduction Innovative and Research Teams Project of Guangdong Pearl River Talents Program (2023ZT10L102), and China Postdoctoral Science Foundation Grant (2024M760587).

■ REFERENCES

(1) Xu, C.; Chen, H.; Liu, Z.; Sui, G.; Li, D.; Kan, H.; Zhao, Z.; Hu, W.; Chen, J. The decay of airborne bacteria and fungi in a constant temperature and humidity test chamber. *Environ. Int.* **2021**, *157*, No. 106816.

(2) Huang, Z.; Yu, X.; Liu, Q.; Maki, T.; Alam, K.; Wang, Y.; Xue, F.; Tang, S.; Du, P.; Dong, Q.; Wang, D.; Huang, J. Bioaerosols in the atmosphere: A comprehensive review on detection methods, concentration and influencing factors. *Sci. Total Environ.* **2024**, *912*, No. 168818.

(3) World Health Organization COVID-19 epidemiological update, edition 163. **2024** 19 January 2024.

(4) Hong, S.; Bhardwaj, J.; Han, C. H.; Jang, J. Gentle sampling of submicrometer airborne virus particles using a personal electrostatic particle concentrator. *Environ. Sci. Technol.* **2016**, *50* (22), 12365−12372.

(5) Yao, M.; Zhang, L.; Ma, J.; Zhou, L. On airborne transmission and control of SARS-Cov-2. *Sci. Total Environ.* **2020**, *731*, No. 139178.

(6) Kim, S. J.; Bae, P. K.; Choi, M.; Keem, J. O.; Chung, W.; Shin, Y. B. Fabrication and application of levan−PVA hydrogel for effective influenza virus capture. *ACS Appl. Mater. Interfaces* **2020**, *12* (26), 29103−29109.

(7) Liu, F.; Ma, Q.; Zhang, J.; Wang, J.; Govindan, D.; Zhao, M.; Gao, C.; Li, Y.; Zhang, W. Self-cleaning microwave-responsive MXene-coated filtration system for enhanced airborne virus disinfection. *ACS Appl. Mater. Interfaces* **2025**, *17* (18), 27167−27177.

(8) Tang, K.; Huang, Z.; Huang, J.; Maki, T.; Zhang, S.; Shimizu, A.; Ma, X.; Shi, J.; Bi, J.; Zhou, T.; Wang, G.; Zhang, L. Characterization of atmospheric bioaerosols along the transport pathway of Asian dust during the Dust-Bioaerosol 2016 Campaign. *Atmos. Chem. Phys.* **2018**, *18*, (10), 7131−7148.

(9) Myung, H.; Joung, Y. S. Contribution of particulates to airborne disease transmission and severity: A review. *Environ. Sci. Technol.* **2024**, *58* (16), 6846−6867.

(10) Qiu, G.; Zhang, X.; deMello, A. J.; Yao, M.; Cao, J.; Wang, J. On-site airborne pathogen detection for infection risk mitigation. *Chem. Soc. Rev.* **2023**, *52* (24), 8531−8579.

(11) Hogan, C. J.; Kettleson, E. M.; Lee, M. H.; Ramaswami, B.; Angenent, L. T.; Biswas, P. Sampling methodologies and dosage assessment techniques for submicrometre and ultrafine virus aerosol particles. *J. Appl. Microbiol.* **2005**, *99* (6), 1422−1434.

(12) Fabian, P.; McDevitt, J. J.; Houseman, E. A.; Milton, D. K. Airborne influenza virus detection with four aerosol samplers using molecular and infectivity assays: considerations for a new infectious virus aerosol sampler. *Indoor Air* **2009**, *19* (5), 433−441.

(13) Tian, Y.; Wu, Y.; Zhang, G.; Chen, H.; Wu, D.; Liu, J.; Li, Y.; Shen, S.; Feng, D.; Pan, Y.; Li, J. Study on the collection efficiency of bioaerosol nanoparticles by andersen-type impactors. *J. Biomed. Nanotechnol.* **2022**, *18* (2), 319−326.

(14) Hospodsky, D.; Yamamoto, N.; Peccia, J. Accuracy, precision, and method detection limits of quantitative PCR for airborne bacteria and fungi. *Appl. Environ. Microbiol.* **2010**, *76* (21), 7004−7012.

(15) Li, J.; Leavey, A.; Wang, Y.; O'Neil, C.; Wallace, M. A.; Burnham, C. A. D.; Boon, A. C.; Babcock, H.; Biswas, P. Comparing the performance of 3 bioaerosol samplers for influenza virus. *J. Aerosol Sci.* **2018**, *115*, 133−145.

(16) Jang, J.; Bhardwaj, J.; Jang, J. Efficient measurement of airborne viable viruses using the growth-based virus aerosol concentrator with high flow velocities. *J. Hazard. Mater.* **2022**, *434*, No. 128873.

(17) Piri, A.; Kim, H. R.; Park, D. H.; Hwang, J. Increased survivability of coronavirus and H1N1 influenza virus under electrostatic aerosol-to-hydrosol sampling. *J. Hazard. Mater.* **2021**, *413*, No. 125417.

(18) Eiguren-Fernandez, A.; Lewis, G. S.; Spielman, S. R.; Hering, S. V. Time-resolved characterization of particle associated polycyclic aromatic hydrocarbons using a newly-developed sequential spot sampler with automated extraction and analysis. *Atmos. Environ.* **2014**, *96*, 125−134.

(19) Pan, M.; Eiguren-Fernandez, A.; Hsieh, H.; Afshar-Mohajer, N.; Hering, S. V.; Lednicky, J.; Hugh Fan, Z.; Wu, C.-Y. Efficient collection of viable virus aerosol through laminar-flow, water-based condensational particle growth. *J. Appl. Microbiol.* **2016**, *120* (3), 805−815.

(20) Yao, M.; Zhang, H.; Dong, S.; Zhen, S.; Chen, X. Comparison of electrostatic collection and liquid impinging methods when collecting airborne house dust allergens, endotoxin and (1, 3)-β-d-glucans. *J. Aerosol Sci.* **2009**, *40* (6), 492−502.

(21) Liu, C.; Hsu, P. C.; Lee, H. W.; Ye, M.; Zheng, G.; Liu, N.; Li, W.; Cui, Y. Transparent air filter for high-efficiency $PM_{2.5}$ capture. *Nat. Commun.* **2015**, *6* (1), No. 6205.

(22) Zhang, R.; Liu, C.; Hsu, P. C.; Zhang, C.; Liu, N.; Zhang, J.; Lee, H. R.; Lu, Y.; Qiu, Y.; Chu, S.; Cui, Y. Nanofiber air filters with high-temperature stability for efficient $PM_{2.5}$ removal from the pollution sources. *Nano Lett.* **2016**, *16* (6), 3642−3649.

(23) Zhang, Y.; Yuan, S.; Feng, X.; Li, H.; Zhou, J.; Wang, B. Preparation of nanofibrous metal−organic framework filters for efficient air pollution control. *J. Am. Chem. Soc.* **2016**, *138* (18), 5785−5788.

(24) Shi, S.; Bai, W.; Chen, X.; Si, Y.; Zhi, C.; Wu, H.; Su, Y.; Cai, W.; Fei, B.; Kan, C.; Hu, J.; Wang, X. Advances in nanofiber filtration membranes: From principles to intelligent applications. *Adv. Funct. Mater.* **2025**, *35* (27), No. 2423284.

(25) Kim, K. S.; Lee, I.; Lee, J. Synergetic chemo-mechano antimicrobial puncturable nanostructures for efficient bioaerosol removal. *BioChip J.* **2024**, *18* (3), 439−452.

(26) Zhang, S.; Liu, H.; Tang, N.; Zhou, S.; Yu, J.; Ding, B. Spider-web-inspired $PM_{0.3}$ filters based on self-sustained electrostatic nanostructured networks. *Adv. Mater.* **2020**, *32* (29), No. 2002361.

(27) Lyu, P.; Ju, Z.; Hu, J.; Pan, H.; Li, X.; Liu, Y.; Ren, J.; Shang, B.; Liu, X.; Xu, W. Heat-resistant air filters based on self-sustained electrostatic and antibacterial polyimide/silver fiber mats. *Adv. Funct. Mater.* **2024**, *34* (29), No. 2400685.

(28) Sánchez-Santolino, G.; Rouco, V.; Puebla, S.; Aramberri, H.; Zamora, V.; Cabero, M.; Cuellar, F. A.; Munuera, C.; Mompean, F.; Garcia-Hernandez, M.; Castellanos-Gomez, A.; Íñiguez, J.; Leon, C.; Santamaria, J. A 2D ferroelectric vortex pattern in twisted $BaTiO_3$ freestanding layers. *Nature* **2024**, *626* (7999), 529−534.

(29) Zhang, Y.; Feng, K.; Song, M.; Xiang, S.; Zhao, Y.; Gong, H.; Ni, F.; Dietrich, F.; Fulanović, L.; Zhuo, F.; Buntkowsky, G.; Frömling, T.; Zhang, D.; Bowen, C.; Rödel, J. Dislocation-engineered piezocatalytic water splitting in single-crystal $BaTiO_3$. *Energy Environ. Sci.* **2025**, *18* (2), 602−612.

(30) Zhao, C.; Gao, Z.; Hong, Z.; Guo, H.; Cheng, Z.; Li, Y.; Shang, L.; Zhu, L.; Zhang, J.; Hu, Z. Ferroelectric and optoelectronic coupling effects in layered ferroelectric semiconductor-based FETs for visual simulation. *Adv. Sci.* **2025**, *12* (11), No. 2413808.

(31) Hemmatpour, H.; De Luca, O.; Crestani, D.; Stuart, M. C. A.; Lasorsa, A.; van der Wel, P. C. A.; Loos, K.; Giousis, T.; Haddadi-Asl, V.; Rudolf, P. New insights in polydopamine formation via surface adsorption. *Nat. Commun.* **2023**, *14* (1), No. 664.

(32) Lee, H.; Dellatore, S. M.; Miller, W. M.; Messersmith, P. B. Mussel-inspired surface chemistry for multifunctional coatings. *Science* **2007**, *318* (5849), 426−430.

https://doi.org/10.1021/acsami.6c09491
ACS Appl. Mater. Interfaces 2026, 18, 41004−41016

(33) Cheng, W.; Zeng, X.; Chen, H.; Li, Z.; Zeng, W.; Mei, L.; Zhao, Y. Versatile polydopamine platforms: synthesis and promising applications for surface modification and advanced nanomedicine. *ACS Nano* **2019**, *13* (8), 8537−8565.
(34) Zhang, C.; Xiang, L.; Zhang, J.; Liu, C.; Wang, Z.; Zeng, H.; Xu, Z. K. Revisiting the adhesion mechanism of mussel-inspired chemistry. *Chem. Sci.* **2022**, *13* (6), 1698−1705.
(35) Lee, K.; Park, M.; Malollari, K. G.; Shin, J.; Winkler, S. M.; Zheng, Y.; Park, J. H.; Grigoropoulos, C. P.; Messersmith, P. B. Laser-induced graphitization of polydopamine leads to enhanced mechanical performance while preserving multifunctionality. *Nat. Commun.* **2020**, *11* (1), No. 4848.
(36) Peng, L.; Wang, H.; Li, G.; Liang, Z.; Zhang, W.; Zhao, W.; An, T. Bioinspired artificial spider silk photocatalyst for the high-efficiency capture and inactivation of bacteria aerosols. *Nat. Commun.* **2023**, *14* (1), No. 2412.
(37) Tian, E.; Liu, J.; Gao, Y.; Mo, J.; Zhang, S.; Bai, X.; Liu, K.; Xu, G.; Liu, K. Artificial polydopamine interface for high-performance ambient particulate matter removal at large velocity. *Carbon Neutralization* **2023**, *2* (2), 245−257.
(38) Liu, H.; Zhang, S.; Liu, L.; Yu, J.; Ding, B. High-performance filters from biomimetic wet-adhesive nanoarchitectured networks. *J. Mater. Chem. A* **2020**, *8* (36), 18955−18962.
(39) Liu, Q.; Yu, B.; Ye, W.; Zhou, F. Highly selective uptake and release of charged molecules by pH-responsive polydopamine microcapsules. *Macromol. Biosci.* **2011**, *11* (9), 1227−1234.
(40) Zong, W.; Hu, Y.; Su, Y.; Luo, N.; Zhang, X.; Li, Q.; Han, X. Polydopamine-coated liposomes as pH-sensitive anticancer drug carriers. *J. Microencapsul.* **2016**, *33* (3), 257−262.
(41) Yu, B.; Wang, D. A.; Ye, Q.; Zhou, F.; Liu, W. Robust polydopamine nano/microcapsules and their loading and release behavior. *Chem. Commun.* **2009**, (*44*), 6789−6791.
(42) Peng, L.; Wang, H.; Li, G.; Zhang, W.; Liang, Z.; An, T. Photocatalytic inactivation of airborne bacteria onto g-C_3N_4/TiO_2/Ni-polydopamine/Ni bifunctional coupling filter with non-size dependent capture effect. *Appl. Catal., B* **2023**, *329*, No. 122580.
(43) Aller, J. Y.; Kuznetsova, M. R.; Jahns, C. J.; Kemp, P. F. The sea surface microlayer as a source of viral and bacterial enrichment in marine aerosols. *J. Aerosol Sci.* **2005**, *36* (5-6), 801−812.
(44) Rinta-Kanto, J. M.; Lehtola, M. J.; Vartiainen, T.; Martikainen, P. J. Rapid enumeration of virus-like particles in drinking water samples using SYBR green I-staining. *Water Res.* **2004**, *38* (10), 2614−2618.
(45) Fu, J.; Chen, Z.; Wang, M.; Liu, S.; Zhang, J.; Zhang, J.; Han, R.; Xu, Q. Adsorption of methylene blue by a high-efficiency adsorbent (polydopamine microspheres): Kinetics, isotherm, thermodynamics and mechanism analysis. *Chem. Eng. J.* **2015**, *259*, 53−61.
(46) Liu, J.; Zhang, J.; Yu, Q.; Liu, Y.; Zhang, X.; Zhu, G.; Jia, Y.; Lu, H.; Gao, J.; Wang, H.; Zhu, B. Flexible, Breathable and hydrophobic SnO_2−SnS_2−SiO_2/SiO_2 all-inorganic self-supporting nanofiber membrane for ultralow-concentration NO_2 sensing under high humidity. *Adv. Funct. Mater.* **2025**, *35* (4), No. 2410833.
(47) Wang, J.; Ying, W.; Lin, B.; Li, C.; Deng, C.; Zhang, H.; Wang, S.; Wang, R. Tillandsia-inspired ultra-efficient thermo-responsive hygroscopic nanofibers for solar-driven atmospheric water harvesting. *Adv. Mater.* **2025**, *37* (3), No. 2408977.
(48) Xiao, S.; Cao, X.; Dong, Z.; Ma, X.; Zhang, X.; Cai, G. A pH-responsive cerium-imidazole decorated ZIF-8 to achieve self-healing barrier property for epoxy coating on Al alloy by controlled release. *Prog. Org. Coat.* **2022**, *163*, No. 106640.
(49) Liu, Y.; Ai, K.; Lu, L. Polydopamine and its derivative materials: synthesis and promising applications in energy, environmental, and biomedical fields. *Chem. Rev.* **2014**, *114* (9), 5057-5115.
(50) Zhang, L.; Li, M.; Tang, C.; Wang, H.; Zhang, X.; Wang, J.; Li, H.; Mahtab, M. S.; Yue, D. Mechanistic insights into the removal of surfactant-like contaminants on mesoporous polydopamine nanospheres from complex wastewater matrices. *Environ. Sci. Technol.* **2024**, *58* (41), 18435−18445.
(51) Njus, D.; Kelley, P. M.; Tu, Y. J.; Schlegel, H. B. Ascorbic acid: The chemistry underlying its antioxidant properties. *Free Radicals Biol. Med.* **2020**, *159*, 37−43.
(52) Ardjani, T. E. A.; Alvarez-Idaboy, J. R. Radical scavenging activity of ascorbic acid analogs: kinetics and mechanisms. *Theor. Chem. Acc.* **2018**, *137* (5), No. 69.
(53) Kesavan, J.; Schepers, D.; McFarland, A. R. Sampling and retention efficiencies of batch-type liquid-based bioaerosol samplers. *Aerosol Sci. Technol.* **2010**, *44*, (10), 817−829.
(54) Bae, J.; Lee, J.; Hwang, W. T.; Youn, D. Y.; Song, H.; Ahn, J.; Nam, J. S.; Jang, J. S.; Kim, D.; Jo, W.; Kim, T. S.; Suk, H. J.; Bae, P. K.; Kim, I. D. Advancing breathability of respiratory nanofilter by optimizing pore structure and alignment in nanofiber networks. *ACS Nano* **2024**, *18* (2), 1371−1380.
(55) Lee, I.; Kim, J.; Kwak, R.; Lee, J. Catalyst droplet-based puncturable nanostructures with mechano-bactericidal properties against bioaerosols. *Adv. Funct. Mater.* **2023**, *33* (26), No. 2213650.

https://doi.org/10.1021/acsami.6c09491
ACS Appl. Mater. Interfaces 2026, 18, 41004−41016